Microchimica Acta (2025) 192:384
https://doi.org/10.1007/s00604-025-07219-5

RESEARCH

A wearable electrochemical aptasensor based MOF on MOF heterostructure for multi-neurotransmitters monitoring

Zina Fredj[1] · Fahimeh Marvi[1] · Fateh Ullah[1] · Mohamad Sawan[1]

Received: 8 March 2025 / Accepted: 4 May 2025 / Published online: 28 May 2025

Abstract

A wearable electrochemical biosensor for real-time monitoring of neurotransmitters in sweat during physical exercise is presented. The biosensor utilizes a CuMOF@InMOF architecture, enhanced with gold nanoparticles (AuNPs), to improve electron transfer, surface area, and overall stability. Thiolate nucleic acid aptamers, highly specific to dopamine, serotonin, and epinephrine, are immobilized on the biosensor surface, enabling precise and simultaneous detection of these key neurotransmitters. The flexible, multi-electrode platform is integrated into a microfluidic patch that adheres to the skin, facilitating seamless sweat collection and continuous neurochemical analysis. Structural validation confirmed the successful synthesis of the CuMOF@InMOF architecture with enhanced surface area, stability, and electron transfer properties, contributing to the biosensor's high sensitivity and selectivity. Impressively, the biosensor achieved detection limits of 0.18 nM for dopamine, 0.33 nM for serotonin, and 0.27 nM for epinephrine, with a broad dynamic range from 1 nM to 10 µM. Performance was validated through square wave voltammetry and amperometry, demonstrating exceptional sensitivity, selectivity, and stability. This innovative biosensor offers a powerful tool for non-invasive, real-time neurochemical monitoring, with significant potential in personalized healthcare.

Highlights

- CuMOF@InMOF obtained using MOF-on-MOF strategy.
- Specific aptamers were loaded on the AuNPs-CuMOF@InMOF structure-based Au–S bond.
- Simultaneous detection of dopamine, serotonin, and epinephrine was achieved.
- Low detection limit with high sensitivity and selectivity was demonstrated.
- Microfluidic module integrated flexible electrode patch for body monitoring.

Keywords Wearable electrochemical biosensor · Neurotransmitter monitoring · CuMOF@InMOF architecture · Gold nanoparticles · Sweat analysis · Aptamer-based detection

Introduction

Depression, an affective disorder, is characterized by persistent feelings of sadness, hopelessness, anhedonia, and, in severe cases, suicidal tendencies. In today's fast-paced lifestyle, it poses a significant challenge to both physical and mental health, contributing to high morbidity and mortality rates [1]. The pathogenesis of depression is widely believed to involve an imbalance in monoamine neurotransmitters (NTs) [2], with deficiencies in these key chemicals being strongly associated with the condition [3]. Antidepressant medications work by increasing the levels of these neurotransmitters, which include epinephrine (EP), serotonin (5-HT), and dopamine (DA). EP, associated with the"fight or flight"response, plays a role in mood regulation and arousal, with disruptions potentially contributing to anxiety and restlessness in depression [4]. 5-HT is crucial in mood regulation, with low levels linked to depressive symptoms, affecting appetite, sleep, and emotional well-being [5]. DA, involved in reward and pleasure, regulates motivation and

✉ Mohamad Sawan
sawan@westlake.edu.cn

[1] CenBRAIN Neurotech, School of Engineering, Westlake University, Hangzhou 310030, China

reinforcement, and imbalances are linked to anhedonia in depression. Given the central role of these NTs in depression, the development of advanced biosensing technologies for their precise detection holds great promise in enhancing both the diagnosis and treatment of psychiatric conditions.

In the pursuit of selective detection for NTs, the limited availability of functional groups for molecular recognition poses a challenge in developing potent receptors for low-weight NTs. Active research continues to focus on creating highly specific bioreceptors capable of detecting various NTs within the living brain [6]. In recent years, aptamers have gained attention as promising bioreceptors for detecting small biomolecules within the brain due to their high binding affinity and selectivity. A number of electrochemical aptasensors have been developed for NTs monitoring, incorporating conductive nanomaterials such as microgel composites to improve performance. However, limitations remain due to the minimal anchoring sites and weak interaction between these nanomaterials and aptamers, which can reduce binding stability. Additionally, substrates currently used for immobilizing aptamers often have limited surface area and sensitivity, and their preparation can be complex. These challenges highlight the need for advanced nanomaterials that can enhance the efficiency and sensitivity of electrochemical aptasensors, ultimately improving their effectiveness in neurotransmitter detection [7]. Real-time detection of 5-HT and DA in the femtomolar range has been achieved using high-affinity aptamers on flexible indium oxide transistors [8]. Graphene field-effect transistors (G-FETs) with aptamers also enable highly sensitive detection, with limits as low as 10 pM [9]. Additionally, gold microelectrode arrays modified with aptamers have been used to detect multiple neurotransmitters, including ATP, DA, and 5-HT [10].

Metal–organic frameworks (MOFs) are highly porous materials with tunable pore sizes and complex nanostructures, making them ideal for biosensing applications [11, 12]. Their large surface areas and chemical functionality enable enhanced biomolecule interaction. Recently, we developed a CeMOF-based aptasensor for monitoring EP with an exceptional sensitivity, achieving an LOD of 0.3 pM [13]. Additionally, a biosensor using a DNA-AuNPs@CuMOF platform for Carcinoembryonic Antigen detection achieved an LOD of 0.25 pg/mL [14]. Elgazar et al. also created a ZIF-8-based biosensor for sensitive COVID-19 RNA detection with an LOD of 6.24 pM [15], highlighting the potential of MOFs in detecting ultra-low biomarker concentrations for early diagnostics. Recent materials science research has focused on MOF-on-MOF architectures, which involve layering different MOF structures to create composites with unique physical and chemical properties [16–18]. These composites offer enhanced flexibility in tuning properties like pore architecture and nanostructuring, improving stability, catalytic activity, and sensing performance[19–21]. Bimetallic MOF-on-MOF structures, incorporating two metals, enhance electronic properties, binding affinity, and structural adaptability, offering improved responsiveness and selectivity for sensitive biomarker detection [22, 23]. Examples include a DA biosensor based on a zinc-cobalt bimetallic MOF with a 3 nM detection limit [24], and a CuZr-MOF-based aptasensor detecting miR-21 with ultra-high sensitivity (0.45 zM) [25]. Additionally, a ZnZr bimetallic MOF-on-MOF-based aptasensor for PTK7 detection achieved an LOD of 0.66 ng/mL [26]. Building on these advances, we report a flexible, wearable electrochemical biosensor for the simultaneous detection of dopamine, epinephrine, and serotonin in sweat. The sensor incorporates a hierarchical CuMOF@InMOF heterostructure, where the InMOF core offers structural integrity and high surface area, while the outer CuMOF shell provides superior conductivity and electrochemical activity. This synergistic MOF-on-MOF architecture enhances electron transfer efficiency and supports sensitive detection. To facilitate aptamer immobilization and further improve electrochemical response, gold nanoparticles (AuNPs) were electrodeposited on the modified electrode surface. Integrated onto a flexible screen-printed patch with a microfluidic sweat collection system, the platform enables real-time, non-invasive monitoring of neurotransmitters. Electrochemical analysis using voltammetry, impedance spectroscopy (EIS), and amperometry confirmed the sensor's excellent sensitivity, selectivity, and reproducibility, highlighting its potential for wearable mental health monitoring applications.

Experimental section

Chemicals and instrumentation

Key chemicals used in this study include indium chloride, copper nitrate, 2-aminoterephthalic acid, and 1,3,5-benzenetricarboxylic acid for MOF synthesis, as well as dopamine, serotonin, epinephrine, and common interferents such as glucose and uric acid. Aptamers specific to each neurotransmitter were obtained from Sangon Biotech. Detailed information on all reagents is provided in the Supplementary Information (SI). Structural characterization was performed using X-ray diffraction (Bruker D8 Discover), SEM (Zeiss Gemini 450), TEM/EDS (Thermo Fisher Talos F200XG2), and XPS (Thermo Fisher ESCALAB Xi +). Electrochemical analysis was conducted using a multichannel potentiostat (BioLogic VMP3) and flexible screen-printed carbon electrodes (SPCEs). Further fabrication and instrumentation details are available in the SI.

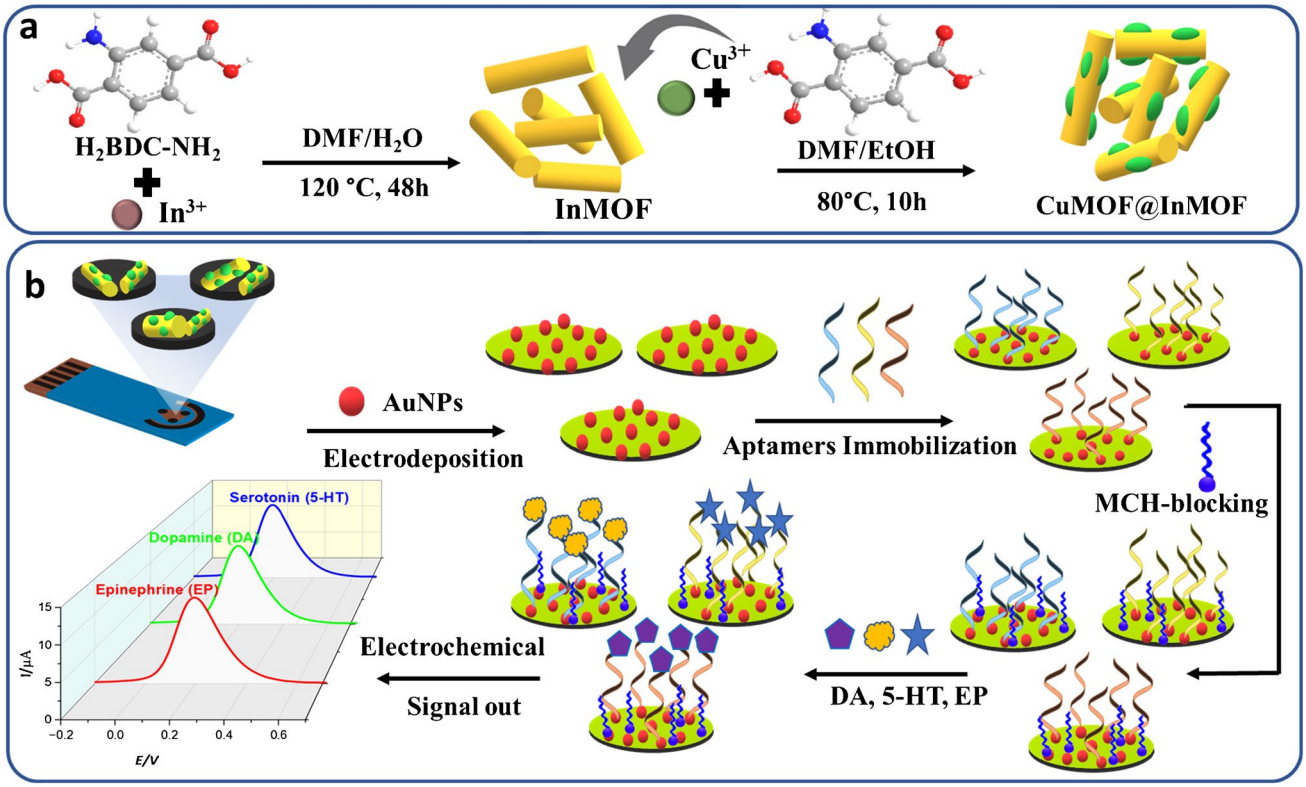

Scheme 1 Biosensor Preparation: **a**) CuMOF@InMOF chemical components and synthesis steps, **b**) Schematic diagram of the multi-neurotransmitters' biosensor based on Aptamers-Coupled AuNPs@CuMOF@InMOF from surface functionalization to signal deliverance

Synthesis of InMOF, CuMOF@InMOF, and CuMOF

The InMOF was synthesized as previously described [27]. A mixture of 80 mg $InCl_3{\cdot}4H_2O$ and 40 mg $H_2BDC\text{-}NH_2$ in 2 mL DMF and 2 mL Milli-Q water was sonicated for 30 min, then heated at 120 °C for 48 h in a Teflon-lined autoclave. The precipitate was washed, vacuum-dried, and yielded InMOF. The CuMOF@InMOF heterojunction was synthesized using an anisotropic growth method (Scheme 1a). Solution A, containing PVP-K30 and InMOF in DMF and ethanol, was mixed with Solution B ($Cu(NO_3)_2$ and $H_2BDC\text{-}NH_2$ in DMF), sonicated, and heated at 80 °C for 8 h. The product was isolated, rinsed with ethanol, and dried. CuMOF was prepared similarly, excluding InMOF. The composite was then drop-casted onto a flexible electrode patch. The fabrication process of the flexible electrode patch is detailed in the SI. Figure S1a illustrates the sequential steps involved in the fabrication, while Figure S1b displays the final dimensions of the assembled flexible electrode patch.

Biosensor preparation

The biosensor fabrication process begins with dispersing 1 mg of CuMOF@InMOF powder in 2 mL of ultrapure water to form a homogeneous suspension, stored at 4 °C for later use. A 5 µL aliquot of this suspension was drop-cast onto the working electrodes surface and allowed to air-dry at room temperature. Once the CuMOF@InMOF-modified electrode surface was prepared, AuNPs were electrodeposited onto it using cyclic voltammetry, applying a voltage range from 0 to 0.8 V at a scan rate of 50 mVs^{-1} over 15 cycles. The electrodeposition process is detailed in the SI, with the cyclic voltammetry (CV) profile shown in Figure S2. This combination of CuMOF@InMOF with AuNPs resulted in a composite material with enhanced electron transfer properties due to the synergistic effects of π-π stacking and coordination interactions. Following AuNP electrodeposition, the modified electrode surface was functionalized with thiolate aptamers specific to dopamine, serotonin, and epinephrine. This functionalization was accomplished through the formation of strong Au–S bonds between the gold nanoparticles and the thiol groups (-SH) of the aptamers. To ensure the biosensor's selectivity and performance, the unmodified areas of the electrode surface were blocked using a 1 mM MCH solution for 40 min to prevent non-specific binding. The neurotransmitter detection mechanism was based on changes in redox peak currents. Upon exposure to neurotransmitters, the aptamers formed highly specific aptamer-neurotransmitter complexes through molecular recognition and hydrogen bonding. This

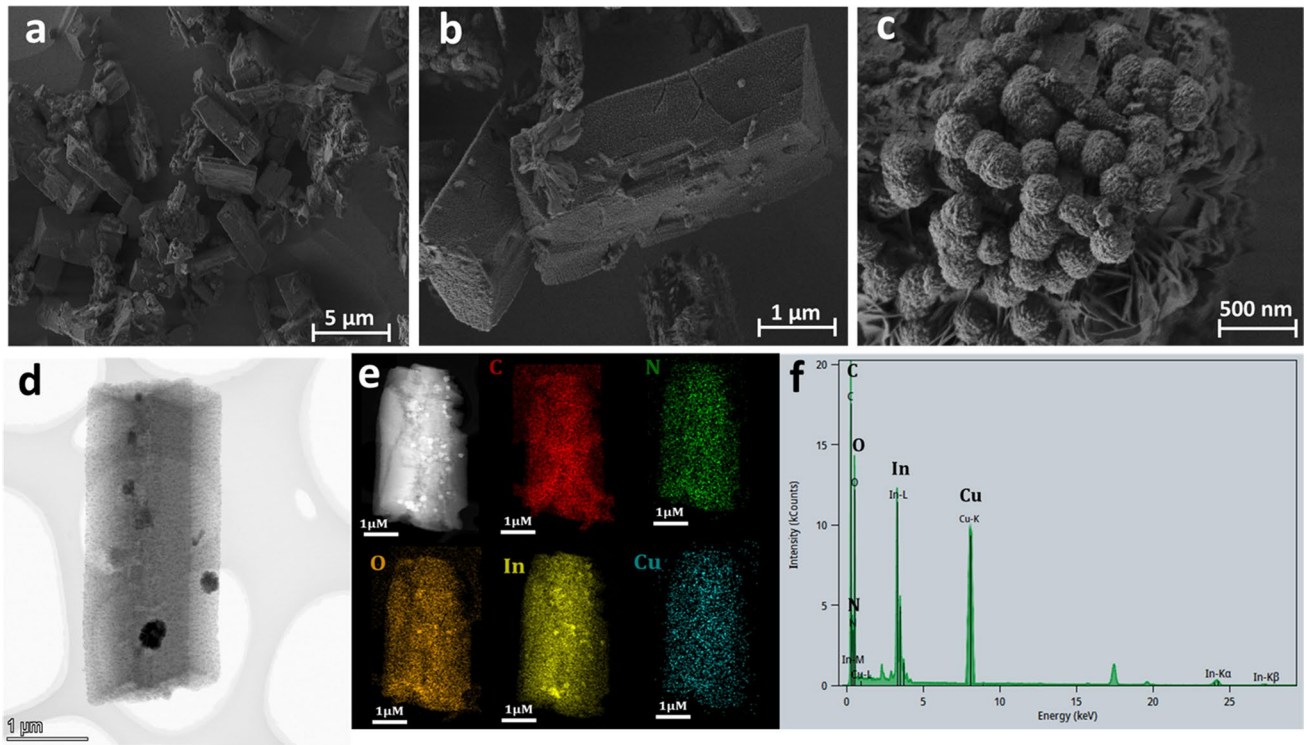

Fig. 1 Morphological characterization: **a**,**b**,**c**) High-magnification SEM with different zoom outs, **d**) HR-TEM, **e**) EDS elemental mapping images, and **f**) EDS spectrum of CuMOF@InMOF

interaction caused conformational changes in the aptamers, which led to a reduction in peak current. The changes in the electrochemical signals were proportional to the concentration of neurotransmitters in the sample, enabling accurate quantification of dopamine, serotonin, and epinephrine. The overall fabrication process and detection mechanism are depicted in Scheme 1b.

Results and discussion

Nanocomposite characterization:

The structural and elemental characteristics of the synthesized CuMOF@InMOF composite were thoroughly examined and are depicted in Fig. 1. SEM images captured at various magnifications (Fig. 1a–c) reveal the morphology and size of the CuMOF@InMOF particles. At lower magnification (Fig. 1a), the image shows a uniform distribution of crystalline particles with average sizes ranging from 1 to 3 µm.

This size uniformity is critical for ensuring reproducibility in biosensing applications. Upon closer inspection (Fig. 1b), the CuMOF crystals exhibit sharp, well-defined rectangular morphologies, suggesting controlled crystal growth and high structural integrity. The higher magnification SEM image (Fig. 1c) highlights the spherical aggregates associated with InMOF, forming a hierarchical microstructure. These spherical structures, with diameters around 500 nm, enhance the overall surface area, facilitating efficient electron transfer and improving sensor performance. To elucidate the morphology of the individual components, SEM images provided in the SI show that InMOF exhibits a rod-like structure (Figure S3a), while CuMOF displays a spherical morphology (Figure S3b), confirming their distinct architectures prior to forming the hierarchical CuMOF@InMOF composite.

The HR-TEM image (Fig. 1d) provides nanoscale insight into the internal structure of the CuMOF@InMOF composite. The image shows a well-organized crystalline lattice with distinct lattice fringes, indicating high crystallinity of the material.

Areas of varying electron density indicate the distribution of copper (Cu), and indium (In) within the MOF framework. The darker regions suggest higher electron density due to the presence of metal atoms, confirming the successful integration of Cu and In metals in the composite. This uniform crystalline structure contributes to the composite's enhanced catalytic activity and stability, which are essential for its application in electrochemical biosensing. Elemental composition and distribution were analyzed using EDS elemental mapping and spectroscopy. The EDS elemental mapping

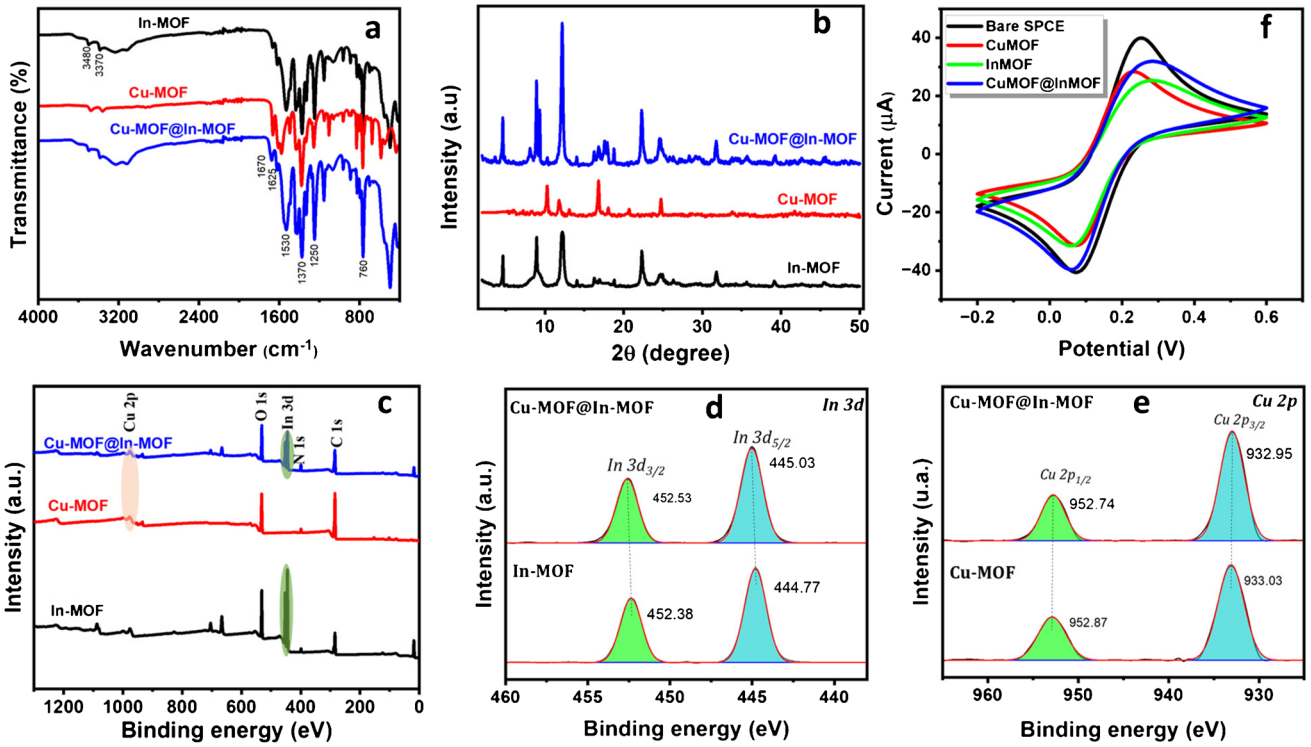

Fig. 2 Structural characterization: **a**) PXRD patterns, **b**) FT-IR spectra, **c**) XPS survey spectra showcasing the structural analysis, and **d**) High-resolution XPS spectra of In 3d for In-MOF and CuMOF@InMOF. **e**) High-resolution XPS spectra of Cu 2p for Cu-MOF and CuMOF@InMOF. **f**) CV plots illustrating the performance of bare SPCE, SPCE/In-MOF, SPCE/Cu-MOF, and SPCE/CuMOF@InMOF

images (Fig. 1e) confirm the homogeneous distribution of carbon (C), nitrogen (N), oxygen (O), Cu, and In throughout the composite material. Each element is represented by a distinct color, and their uniform overlap indicates successful synthesis of the CuMOF@InMOF heterostructure. The co-localization of Cu and In elements suggests strong interaction between the CuMOF and InMOF components, which is anticipated to enhance electron transfer efficiency and provide synergistic effects in catalytic activity. The EDS spectrum (Fig. 1f) further verifies the elemental composition of the composite. Distinct peaks corresponding to C, N, O, Cu, and In are clearly observed, with no significant impurity peaks detected.

This confirms the purity of the synthesized material, which is vital for ensuring consistent and reliable performance in biosensing applications. The presence of C, N, and O also indicates the organic linker components of the MOFs, which play a critical role in the structural integrity and functionality of the composite. All the analyses confirm the successful synthesis of a CuMOF@InMOF composite with a well-defined crystalline structure and uniform elemental distribution. The hierarchical architecture observed in the SEM images, combined with the homogeneous elemental distribution from EDS mapping, suggests that the composite has a high surface area and enhanced electron transfer properties. These features are expected to contribute significantly to the improved sensitivity, selectivity, and stability of the electrochemical biosensor for neurotransmitter detection.

The structural and electrochemical properties of the CuMOF@InMOF composite were extensively characterized using PXRD, FT-IR, XPS, and electrochemical impedance spectroscopy (EIS). The PXRD patterns (Fig. 2a) reveal prominent diffraction peaks for CuMOF at $2\theta = 10.2°$, 14.6°, and 17.3°, corresponding to the (011), (110), and (112) planes, respectively, which confirm the well-defined crystalline structure of CuMOF. Upon the integration of InMOF, the composite CuMOF@InMOF displays additional peaks at $2\theta = 12.5°$ and 16.1°, indicating the successful incorporation of InMOF while maintaining the overall crystallinity of the material. This suggests that the two MOFs coexist harmoniously without structural disruption, which is crucial for maintaining high surface area and stability in biosensor applications. The FT-IR spectra (Fig. 2b) provide further confirmation of the structural integrity and functional groups in the composite. CuMOF exhibits strong absorption bands at 1620 cm^{-1} due to the C = O stretching vibration of the carboxylate groups, and at 1380 cm^{-1}, corresponding to C–N stretching. In the CuMOF@InMOF composite, new absorption bands appear at 3350 cm^{-1}, attributed to O–H stretching from InMOF, indicating the presence of hydroxyl

groups or adsorbed moisture, which could further enhance the material's hydrophilicity and interaction with analytes in biosensing applications. Additionally, shifts in the C = O and C–N bands suggest strong coordination between Cu and In metals with the organic ligands, confirming the robust formation of the composite.

The XPS survey spectra (Fig. 2c) provides insight into the elemental composition of CuMOF@InMOF, with characteristic peaks for Cu 2p, In3 d, C 1 s, O 1 s, and N 1 s. The high-resolution XPS spectrum of In3 d (Fig. 2d) reveals the In3 $d_5/_2$ peak at 445.2 eV and In 3 $d_3/_2$ at 452.7 eV, confirming the presence of In^{3+} in the composite. Similarly, high-resolution XPS spectra of Cu 2p (Fig. 2e) shows the Cu $2p_3/_2$ peak at 934.2 eV and Cu $2p_1/_2$ at 954.1 eV, along with satellite peaks, indicating the presence of Cu^{2+} in the composite. These values are consistent with the expected oxidation states of Cu and In in their respective MOFs, suggesting a successful formation of the CuMOF@InMOF hybrid with strong metal–ligand interactions. In addition, cyclic voltammetry was employed to analyze the electrochemical properties of different MOF-modified electrode configurations, as shown in Fig. 2f. Interestingly, the modification of the electrode with individual MOFs, CuMOF and InMOF, resulted in a decrease in current compared to the bare electrode. This reduction can be attributed to the inherent low conductivity of MOF materials, which limits electron transfer. Between the two-single MOF modifications, CuMOF exhibited a slightly higher current response than InMOF. This difference is likely due to the superior conductivity of copper, which provides better electron mobility and thus marginally enhances the electrochemical performance compared to InMOF. The CuMOF@InMOF heterostructure showed a significant improvement in current response compared to individual MOF modifications. This enhancement is due to better conductivity, increased electroactive surface area, and optimized electron pathways. The synergistic effect of combining CuMOF and InMOF provides a more extensive network of active sites, leading to more efficient redox reactions.

Cyclic voltammetry data for the different electrode modifications: bare SPCE (Fig. 3a), CuMOF@InMOF-modified SPCE (Fig. 3b), and AuNPs-CuMOF@InMOF-modified SPCE (Fig. 3c), were analyzed across a range of scan rates to determine the electroactive surface area (ECSA) using the Randles–Sevcik Eq. (E1). The inset plots in Fig. 3a, b, and c show the relationship between the anodic peak current (Ipa) and the square root of the scan rate ($\upsilon^{1/2}$) as well as the cathodic peak current (Ipc) for each electrode configuration. The linearity of these plots indicates that the redox process is diffusion-controlled for all electrode modifications:

$$Ip = \left(2.69 * 10^5\right) n^{3/2} A {D_0}^{1/2} v^{1/2} C_0^* \quad (1)$$

Ip refers to the anodic peak current, n is the number of electron transferred during the electrode reaction, A is the surface area of the electrode, D_0 is the diffusion coefficient i.e. 7.6×10^{-6} cm^2 s^{-1}, ν is the scan rate and C_0* is the concentration of $K_3Fe(CN)_6/K_4Fe(CN)_6$ solution.

The calculated ECSA values are approximately 0.029 cm^2 for the bare SPCE, 0.047 cm^2 for the CuMOF@InMOF modification, and 0.071 cm^2 for the AuNPs-CuMOF@InMOF modification. These results confirm that each successive modification enhances the electrochemical surface area, providing improved electron transfer capabilities. The increased ECSA plays a critical role in enhancing the biosensor's sensitivity. A larger electroactive surface area provides more active sites for aptamer immobilization and redox reactions of target neurotransmitters. This facilitates efficient electron transfer at the electrode–electrolyte interface, reduces charge transfer resistance, and enhances the sensing surface's catalytic activity. These synergistic effects contribute to the improved current response and lower detection limits observed in the developed biosensor.

The sequential modification of the biosensor was analyzed using EIS to monitor the impact of each functionalization step on the charge transfer resistance R_{ct}. Measurements were conducted in a 5.0 mM ferricyanide redox couple $K_3Fe(CN)_6/K_4Fe(CN)_6$ solution using a potentiostat, with EIS data collected over a frequency range of 100 kHz to 100 mHz. is consistent with the formation of a selective and stable interface on the electrode surface. Nyquist plots were generated to monitor impedance changes at each electrode modification step, where the semicircle diameter reflects the charge transfer resistance (R_{ct}), an indicator of electron transfer efficiency at the electrode surface. The data were fitted using a Randles equivalent circuit model comprising solution resistance (R_s), charge transfer resistance (R_{ct}), double-layer capacitance (C_{dl}), and Warburg impedance (Z_w), as illustrated in the inset of Fig. 3d. Initially, the bare SPCE exhibited the highest Rct (~ 300 Ω), indicating poor electron transfer. Modification with CuMOF@InMOF reduced R_{ct} to ~ 250 Ω due to its porous structure and improved conductivity. Further incorporation of AuNPs lowered the R_{ct} to ~ 220 Ω, highlighting the enhanced electron transfer resulting from the highly conductive gold nanoparticles. Subsequent aptamer immobilization increased R_{ct} to ~ 280 Ω, as the insulating aptamer layer introduces a kinetic barrier to electron flow. Finally, functionalization with MCH raised R_{ct} further to ~ 340 Ω, consistent with the formation of a dense passivation layer that blocks nonspecific binding and stabilizes the sensing surface. These results confirm that each modification step is traceable via EIS and demonstrate the sensor's progressive functionalization and selective surface preparation.

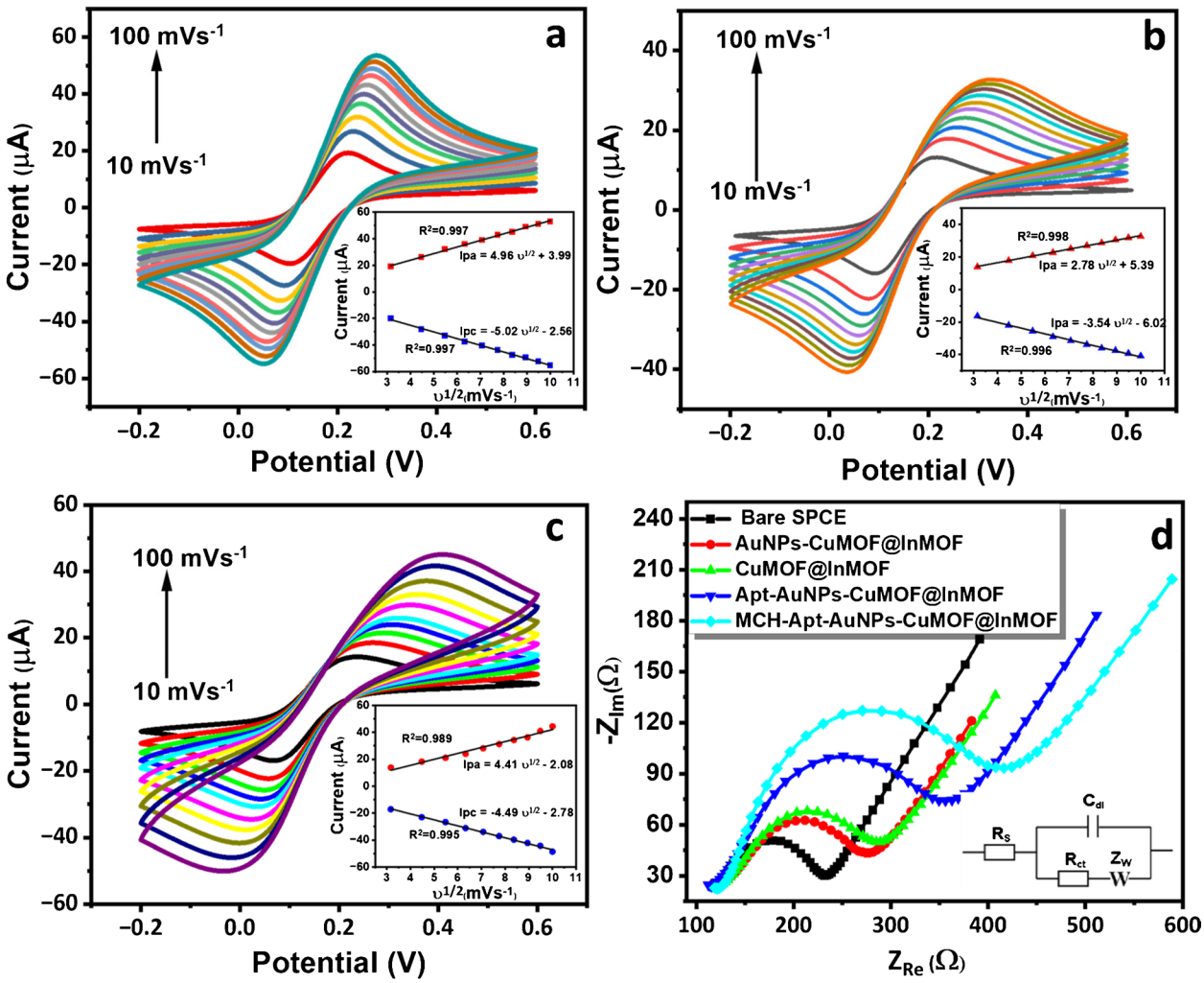

Fig. 3 Electrochemical characterization of various electrode modifications using CV and EIS: **a**) CV analysis of the bare SPCE electrode, **b**) SPCE modified with CuMOF@InMOF, **c**) SPCE further modified with AuNPs-CuMOF@InMOF for different scan rates from 10 mV/s to 100 mV/s. The insets show the linear relationship between anodic (Ipa) and cathodic (Ipc) peak currents and the square root of the scan rate, and **d**) EIS analysis of the electrodes at different stages of functionalization, illustrating changes in charge transfer resistance (R_{ct}) based on electrode modification

Dopamine monitoring

To monitor the electrochemical response of the biosensor against dopamine, we used square wave voltammetry (SWV) and amperometry under optimized conditions, as illustrated in Fig. 4. The SWV results (Fig. 4a), recorded with an amplitude of 5 mV and a frequency of 20 Hz, exhibit a well-defined oxidation peak for dopamine at approximately 0.2 V. As the dopamine concentration increased from 1 nM to 10 µM, the oxidation peak current gradually rose, reflecting the biosensor's high sensitivity to dopamine. The CuMOF@InMOF-modified electrode, enhanced with AuNPs, facilitated efficient electron transfer, contributing to the clear and well-defined peaks, which demonstrate the sensor's robustness across a broad concentration range. To further validate the biosensor's performance, amperometric measurements were carried out at a constant potential of 0.35 V in artificial sweat (pH 6.5) (Fig. 4b). This potential was selected to ensure complete oxidation and a stable current response. The resulting amperometric current increased linearly with dopamine concentration, confirming the sensor's suitability for real-time monitoring.

The selectivity of the biosensor was evaluated using 100 nM concentrations of common interferents, including glucose, norepinephrine, serotonin, epinephrine, and acetylcholine (Fig. 4c). The results show that the biosensor exhibited a significantly higher current response for dopamine, while the responses to other analytes were minimal, as displayed in the histogram comparing the percentage response of dopamine with potential interferents. The inset shows the

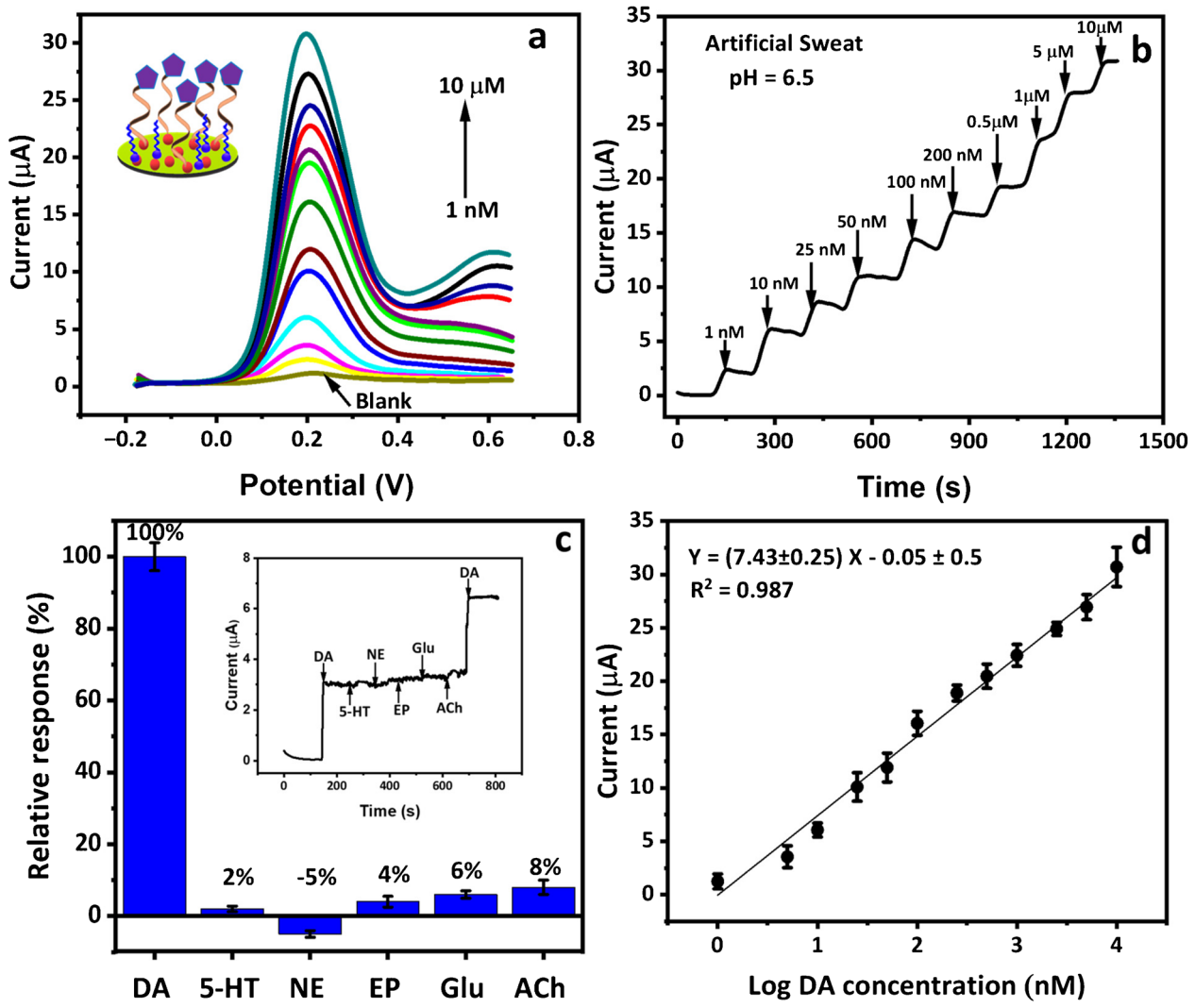

Fig. 4 Dopamine Biosensor analytical performances: **a**) SWV response curves of the CuMOF@InMOF/AuNP-modified biosensor for various dopamine concentrations. **b**) Amperometric response of the biosensor at a fixed potential of 0.35 V for increasing dopamine concentrations, **c**) Histogram comparing the percentage response of dopamine with potential interferents (Inset: amperometric response of the biosensor after injection of dopamine and interferents), and **d**) Calibration curve showing the relationship between dopamine oxidation peak current and concentration, ranging from 1 nM to 10 μM

amperometric response of the biosensor following the injection of dopamine and the respective interferents. This strong selectivity arises from the high binding affinity between dopamine and the surface-immobilized aptamers, combined with the improved electron transfer efficiency provided by the CuMOF@InMOF/AuNPs composite. Figure 4d shows a linear relationship between the oxidation peak current and the logarithmic concentration of dopamine with the equation $Y = (7.43 \pm 0.25)\ X—0.05 \pm 0.5$ and a coefficient of determination R^2 of 0.987, based on SWV measurements. The LOD was calculated to be 0.18 nM (defined as 3σ/slope, where σ is the standard deviation of blank measurements), highlighting the biosensor's high sensitivity for detecting low dopamine concentrations. Furthermore, with a relative standard deviation (RSD) of 3.28%, the biosensor demonstrated excellent reproducibility and stability, making it ideal for continuous monitoring applications.

Serotonin monitoring

The sensitivity of the aptasensor was explored through SWV measurements, as shown in Fig. 5a. The SWV responses exhibited well-defined oxidation peaks for serotonin at around 0.3 V over a concentration range of 1 nM to 10 μM. The peak current increased proportionally with serotonin concentration, highlighting the excellent sensitivity of the aptasensor. This linear response, especially at low concentrations, demonstrates the potential for detecting serotonin

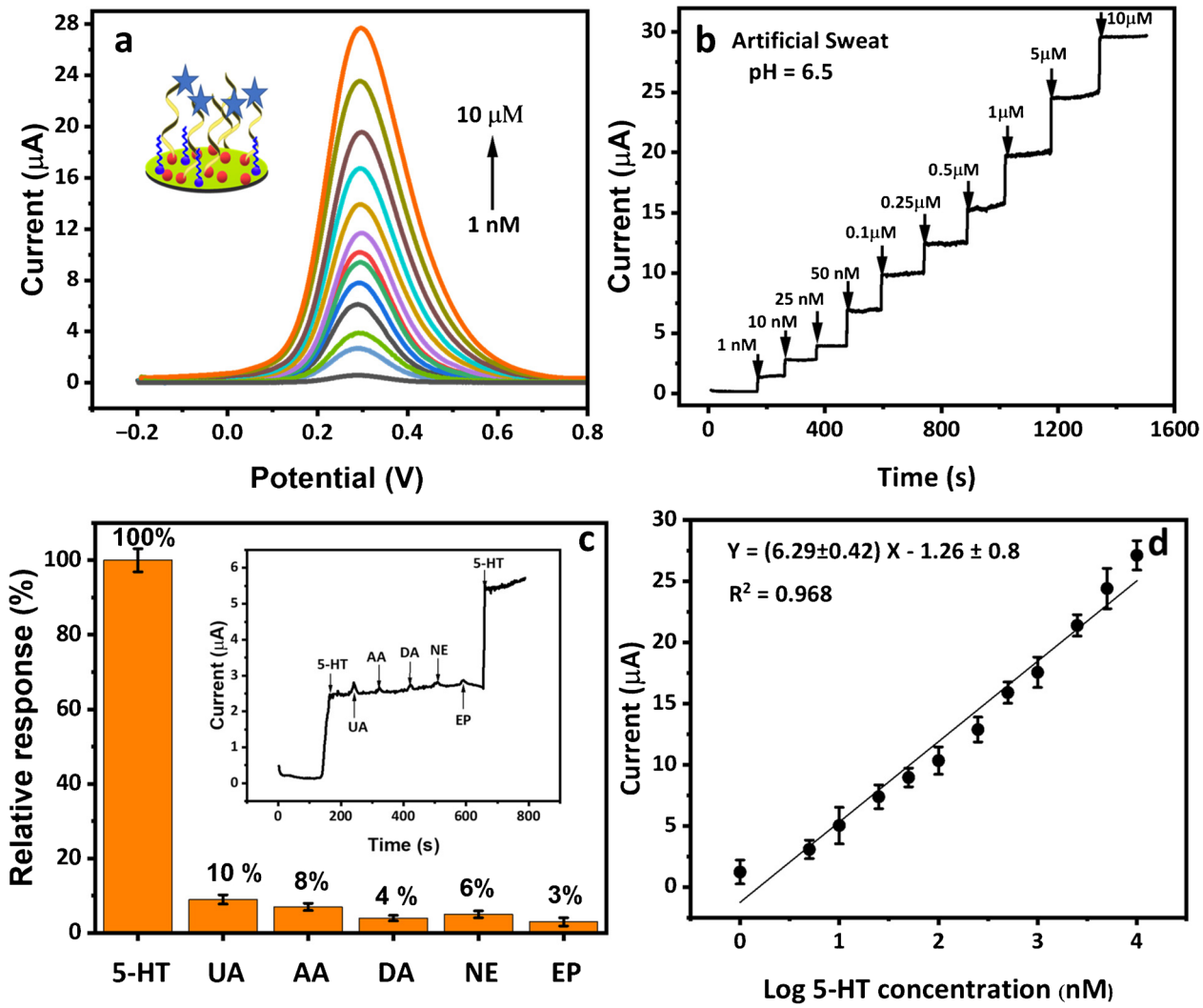

Fig. 5 Serotonin Monitoring: **a**) SWV responses of the sensor for serotonin detection at varying concentrations (1 nM to 10 μM), **b**) Amperometric detection of serotonin in artificial sweat (pH 6.5), demonstrating a stepwise increase in current with rising concentrations from 1 nM to 10 μM, confirming the sensor's high sensitivity in physiological conditions, **c**) Histogram of the biosensor's relative response (%) to serotonin and common interferents (uric acid, ascorbic acid, dopamine, norepinephrine, and epinephrine). The inset displays the amperometric signals corresponding to each analyte, and **d**) Calibration curve obtained from SWV measurements for serotonin

at trace levels, making this system suitable for real-time monitoring applications in wearable devices. Amperometric measurements, presented in Fig. 5b, further confirmed the sensor's capability to detect serotonin in physiological conditions. The current response in artificial sweat increased in discrete steps as serotonin concentrations were raised from 1 nM to 10 μM. This confirms the aptasensor's high sensitivity across a wide concentration range, allowing for accurate monitoring in complex biological environments. Selectivity studies were performed using 100 nM concentrations of common interferents, including uric acid, ascorbic acid, dopamine, norepinephrine, and epinephrine, to assess the biosensor's specificity. As illustrated in Fig. 5c, serotonin exhibited the highest relative response at 100%, while the other analytes showed significantly lower responses, below 20%. This indicates that the aptasensor demonstrates acceptable selectivity for serotonin due to the specific binding properties of the aptamer. The inset of Fig. 5c shows the corresponding amperometric signals for each analyte, demonstrating clear peak separation and further confirming the biosensor's robustness against interference. To quantify the sensor's analytical performance, a calibration curve was generated from SWV data, as shown in Fig. 5d.

The curve exhibits a linear relationship between the logarithmic concentration of serotonin and the current response within the range of 1 nM to 10 μM, with the equation $Y = (6.29 \pm 0.42)\ X — 1.26 \pm 0.8$ and a correlation coefficient R^2 of 0.968. The limit of detection was calculated to be 0.33

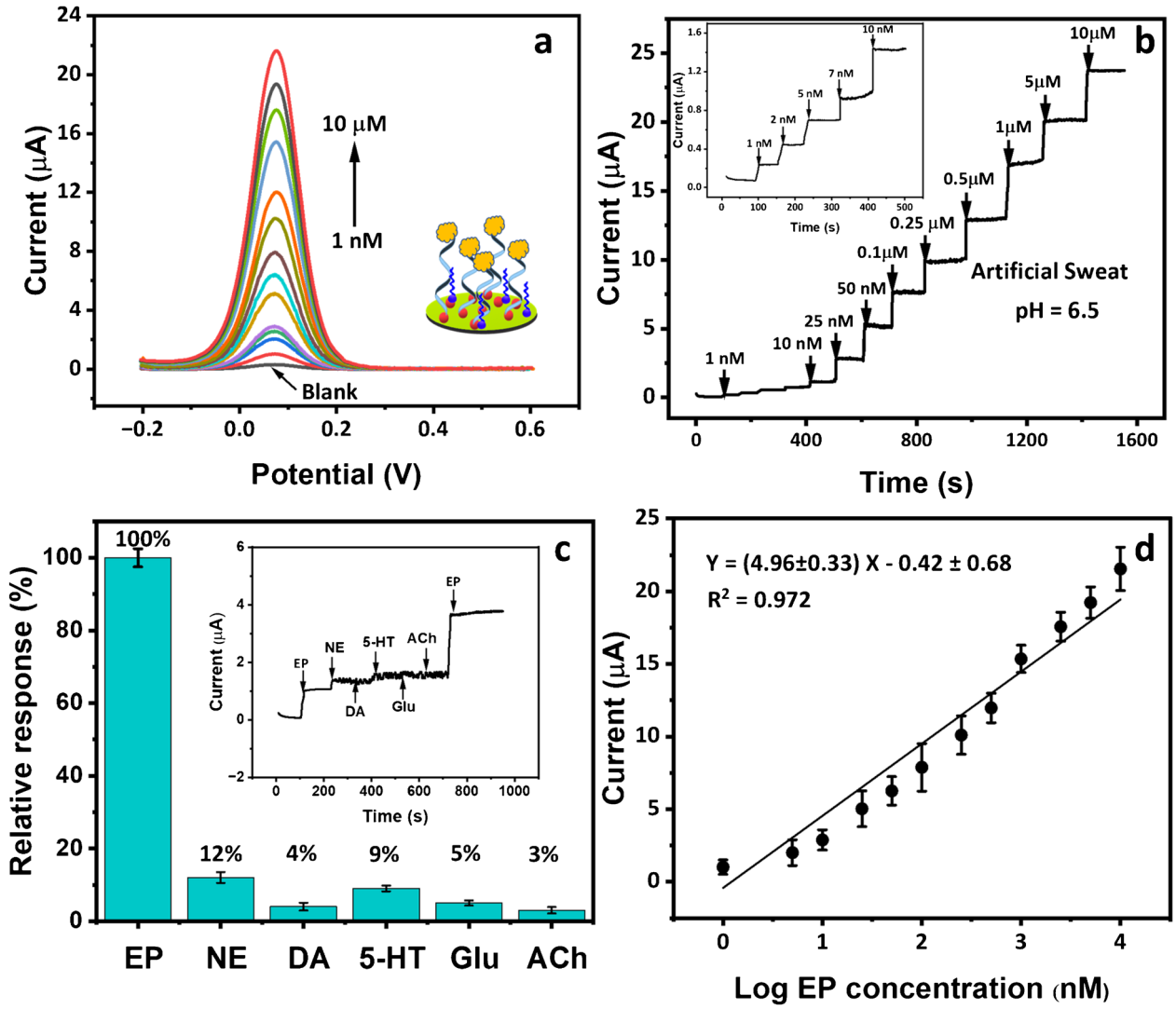

Fig. 6 Epinephrine Monitoring: **a**) SWV responses for epinephrine at various concentrations. **b**) Amperometric detection in artificial sweat with inset zooms in on the low-concentration range, showcasing the sensor's sensitivity from 1 to 10 nM. **c**) Histogram compares sensor responses to epinephrine and interfering molecules, with epinephrine showing a 100% response. The inset confirms selectivity via amperometric curves. (**d**) Calibration curve shows a linear relationship between concentration and current response

nM, indicating the sensor's capacity to detect ultra-low concentrations of serotonin. Additionally, RSD was determined to be 4.56%, confirming the sensor's precision and reproducibility.

Epinephrine monitoring

In addition to dopamine and serotonin, the developed wearable aptasensor was also employed for the detection of epinephrine. The sensor's performance was characterized through SWV and amperometry. Figure 6a presents the SWV results for epinephrine detection across concentrations ranging from 1 nM to 10 μM. The sensor displays a clear oxidation peak around 70 mV, with the peak current increasing linearly as the concentration rises. This demonstrates the sensor's exceptional sensitivity, particularly at low concentrations, which is essential for its application in real-time wearable biosensors. The corresponding amperometric measurements in artificial sweat show a stepwise increase in current with each successive addition of epinephrine (Fig. 6b). This progressive response reflects the sensor's ability to reliably track concentration changes in real time. Notably, the inset in Fig. 6b zooms in on the low-concentration range, showcasing the sensor's responsiveness to even minimal changes in epinephrine concentration between 1 and 10 nM. This further validates the sensor's capability for precise detection in physiologically relevant environments.

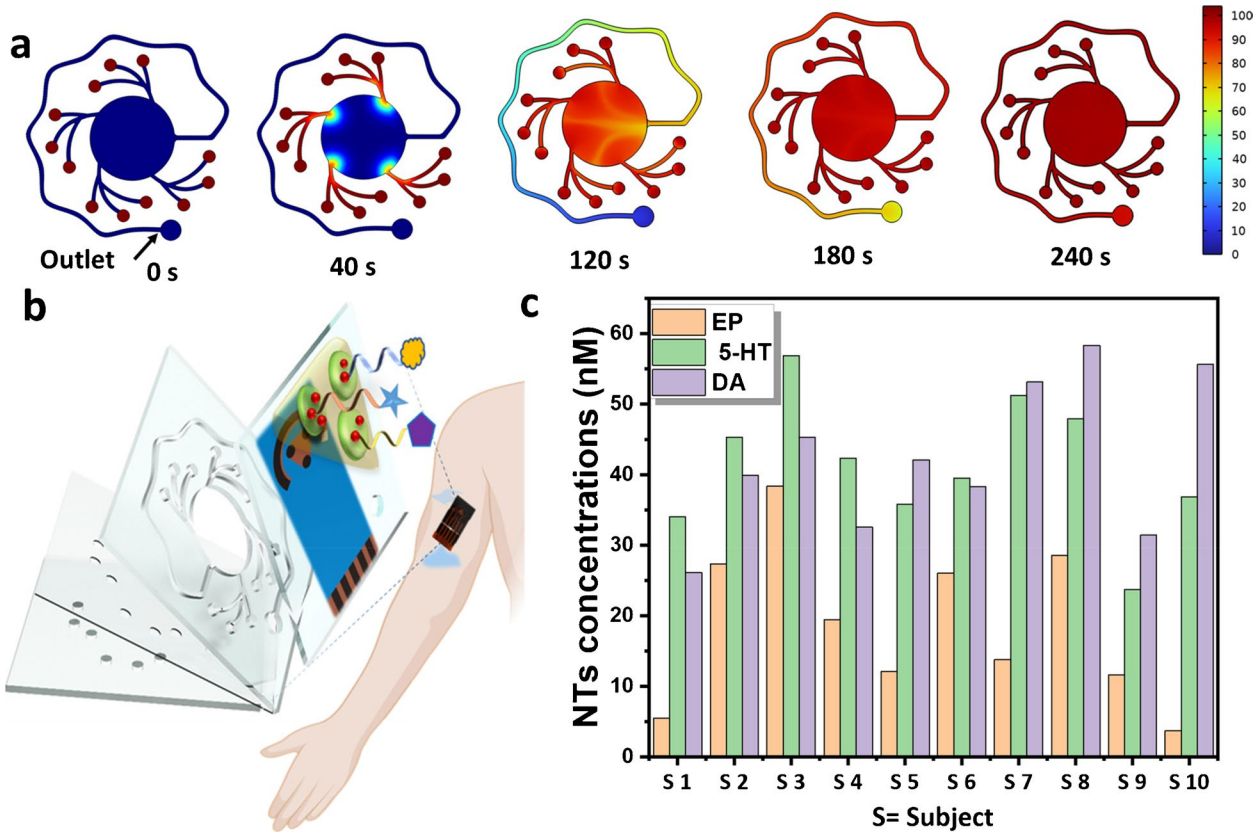

Fig. 7 On body monitoring: **a**) Simulations of solute concentration distributions on the bottom surface of the microfluidic chamber over time, illustrating the dynamic diffusion and interaction of analytes within the microfluidic environment. The progression is shown at distinct time intervals, with the color scale representing concentration levels from low (blue) to high (red), **b**) Schematic representation of the wearable biosensor system applied on the forearm for neurotransmitter monitoring. The system integrates a microfluidic channel with a flexible electrode platform for real-time sweat collection and analysis, and **c**) NTs concentrations (EP, 5-HT, and DA) measured in sweat samples from 10 healthy volunteers aged 27–40 after exercise, based on calibration-derived values

Figure 6c presents an interference study in which the sensor's response to 0.1 µM epinephrine is compared with those of norepinephrine, dopamine, serotonin, glucose, and acetylcholine, all tested at 100 nM. Epinephrine achieves a 100% relative response, while the other analytes display significantly lower responses, with the highest interferent response being norepinephrine at 12%. The inset of Fig. 6c shows the corresponding amperometric curves for each analyte, reinforcing the sensor's selectivity by highlighting the clear separation of the epinephrine signal from other substances. Finally, the calibration curve in Fig. 6d demonstrates the linear relationship between the logarithmic concentration of epinephrine and the current response. The sensor maintains linearity from 1 nM to 10 µM, with a regression equation of $Y = (4.96 \pm 0.33) X - 0.42 \pm 0.68$ and an R^2 value of 0.972. The LOD is calculated as 0.27 nM, and the RSD is 5.26%, highlighting the sensor's precision and reproducibility for real-world applications.

On body neurotransmitters monitoring

To enable real-time, non-invasive monitoring of neurotransmitters in sweat, we developed a wearable platform that integrates a flexible electrode array with a custom-designed, multilayered microfluidic module. Designed in AutoCAD and fabricated using CO_2 laser cutting, the module includes a central chamber (radius: 6.0 mm) connected to twelve inlets and one outlet to ensure efficient and uniform sweat collection (Figure S4). It comprises three layers: an adhesive layer, a PET spacer, and a patterned PET channel layer, all assembled and aligned with the biosensor for stable operation during wear (Figure S5). The system operates passively, relying on naturally generated sweat during physical activity, and does not require external pumping or flow control. The microfluidic geometry was specifically engineered to minimize clogging and maintain consistent flow to the sensing area. Detailed fabrication procedures and material specifications are provided in the Supplementary Information. This design enables continuous analyte transport and direct analysis of raw sweat samples

without pre-concentration, making it well-suited for wearable electrochemical sensing.

Simulations using COMSOL (Fig. 7a) demonstrate solute concentration dynamics within the microfluidic chamber over time, validating the system's ability to achieve effective diffusion and interaction of analytes. Figure 7b illustrates the wearable biosensor's integration onto the forearm, enabling real-time sweat collection and neurotransmitter monitoring during physical activity.

On-body validation was conducted with 10 healthy volunteers (aged 27–40) during physical activity. As shown in Figure S6a and S6b, the flexible biosensor patch was applied to the forearm before exercise, and connected post-exercise to a multichannel potentiostat. SWV signals were simultaneously acquired across three channels (Figure S6c), each corresponding to a working electrode functionalized for epinephrine, dopamine, or serotonin detection. The SWV curves measured from the sweat samples of all 10 volunteers are presented in Figure S7. The corresponding peak currents were projected onto standard calibration curves established in synthetic sweat to quantify the concentrations of each neurotransmitter. The calculated concentrations of epinephrine, serotonin, and dopamine are presented in Fig. 7c. The results highlight the biosensor's capability to provide accurate, real-time neurotransmitter monitoring, demonstrating its potential for real-world applications. Our sensor shows competitive LODs for DA, 5-HT, and EP in sweat, as highlighted in Table S2, outperforming many studies in similar or more complex matrices. While some studies have lower LODs under controlled conditions, our sensor balances sensitivity with practicality, making it ideal for wearable applications. This approach offers versatility and robustness for real-time, on-body neurotransmitter monitoring.

Conclusion

We introduced an innovative wearable electrochemical biosensor for the real-time, continuous monitoring of neurotransmitters in sweat during physical activity. The sensor integrates a flexible, multi-electrode array into a microfluidic patch, enabling efficient sweat collection and seamless neurochemical analysis directly on the skin. The biosensor is built on a CuMOF@InMOF heterostructure, enhanced with AuNPs, which significantly improves electron transfer, surface area, and overall stability. To achieve simultaneous and selective detection of dopamine, serotonin, and epinephrine, thiolated nucleic acid aptamers, specific to each neurotransmitter, were immobilized on the sensor surface. Material characterization techniques, including SEM, HRTEM-EDS, XRD, and XPS, confirmed the robust structural integrity of the sensor, while amperometry and square wave voltammetry validated its electrochemical performance. The biosensor demonstrated outstanding sensitivity, with detection limits of 0.18 nM for dopamine, 0.33 nM for serotonin, and 0.27 nM for epinephrine, across a broad dynamic range from 1 nM to 10 μM. Additionally, finite element simulations were employed to optimize both the electrode geometry and fluid dynamics within the microfluidic system, further enhancing the sensor's performance and efficiency. This novel biosensor represents a significant advancement in non-invasive, real-time neurochemical monitoring, with potential applications in personalized healthcare, mental health diagnostics, and neurophysiological studies. Looking ahead, future work will focus on developing a fully wireless, battery-free version of this biosensor, leveraging energy harvested from biochemical reactions to power the device, thereby advancing towards continuous, autonomous monitoring systems.

Supplementary Information The online version contains supplementary material available at https://doi.org/10.1007/s00604-025-07219-5.

Authors contributions Z.F: Methodology, experiments, data analysis, writing the draft, validation. F. M.: Simulation, validation. F.U: Material characterization. M.S: Supervision, reviewing and editing, resources. All authors reviewed the manuscript.

Funding This work was supported by Westlake University, Leading Innovative and Entrepreneur Team Introduction Program of Zhejiang (grant number 2020R01005), and the National Natural Science Foundation of China [Grant No. W2431058].

Data availability No datasets were generated or analysed during the current study.

Declarations

Ethical approval All participants were informed and agreed to cooperate fully with the completion of this study.

Consent to participate Informed consent was obtained from all participants.

Consent to publish All participants consented to the publication of their data.

Competing interests The authors declare no competing interests.

References

1. Chandrasekhar Y, Ramya EM, Navya K et al (2017) Antidepressant like effects of hydrolysable tannins of *Terminalia catappa* leaf extract *via* modulation of hippocampal plasticity and regulation of monoamine neurotransmitters subjected to chronic mild stress (CMS). Biomed Pharmacother 86:414–425. https://doi.org/10.1016/j.biopha.2016.12.031
2. Xing H, Zhang X, Xing N et al (2019) Uncovering pharmacological mechanisms of Zhi-Zi-Hou-Po decoction in chronic unpredictable mild stress induced rats through pharmacokinetics, monoamine neurotransmitter and neurogenesis. J Ethnopharmacol 243:112079. https://doi.org/10.1016/j.jep.2019.112079
3. Ma M, Quan H, Chen S et al (2023) The anxiolytic effect of polysaccharides from stellariae radix through monoamine neurotransmitters, HPA Axis, and ECS/ERK/CREB/BDNF signaling pathway in stress-induced male rats. Brain Res Bull 203:110768. https://doi.org/10.1016/j.brainresbull.2023.110768
4. Ford V, Applefeld W, Wang J et al (2022) Early epinephrine infusion prevents late myocardial depression and accelerates cardiac recovery in a large animal model of septic shock. J Am Coll Cardiol 79:271. https://doi.org/10.1016/S0735-1097(22)01262-1
5. Zhao S, Piatkevich KD (2023) Techniques for in vivo serotonin detection in the brain: State of the art. J Neurochem 166:453–480. https://doi.org/10.1111/jnc.15865
6. Hu Z, Li Y, Figueroa-Miranda G et al (2023) Aptamer based biosensor platforms for neurotransmitters analysis. TrAC, Trends Anal Chem 162:117021. https://doi.org/10.1016/j.trac.2023.117021
7. Stuber A, Nakatsuka N (2024) Aptamer Renaissance for Neurochemical Biosensing. ACS Nano 18:2552–2563. https://doi.org/10.1021/acsnano.3c09576
8. Liu Q, Zhao C, Chen M et al (2020) Flexible Multiplexed In2O3 Nanoribbon Aptamer-Field-Effect Transistors for Biosensing. iScience 23:101469. https://doi.org/10.1016/j.isci.2020.101469
9. Gao Z, Wu G, Song Y et al (2022) Multiplexed monitoring of Neurochemicals via Electrografting-enabled site-selective functionalization of aptamers on field-effect transistors. Anal Chem 94:8605–8617. https://doi.org/10.1021/acs.analchem.1c05531
10. Sen D, Lazenby RA (2023) Selective aptamer modification of au surfaces in a microelectrode sensor array for simultaneous detection of multiple analytes. Anal Chem 95:6828–6835. https://doi.org/10.1021/acs.analchem.2c05335
11. He J, He J, Tang L et al (2024) Rapid in-situ synthesis of metal organic frameworks for biosensors. TrAC, Trends Anal Chem 175:117709. https://doi.org/10.1016/j.trac.2024.117709
12. Yang Z-W, Li J-J, Wang Y-H et al (2023) Metal/covalent-organic framework-based biosensors for nucleic acid detection. Coord Chem Rev 491:215249. https://doi.org/10.1016/j.ccr.2023.215249
13. Fredj Z, Wang P, Ullah F, Sawan M (2023) A nanoplatform-based aptasensor to electrochemically detect epinephrine produced by living cells. Microchim Acta 190:343. https://doi.org/10.1007/s00604-023-05902-z
14. Bahri M, Fredj Z, Qin P, Sawan M (2024) DNA-Coupled AuNPs@CuMOF for sensitive electrochemical detection of carcinoembryonic antigen. ACS Appl Nano Mater 7:11921–11930. https://doi.org/10.1021/acsanm.4c01473
15. Elgazar A, Sabouni R, Ghommem M, Majdalawieh AF (2024) Novel metal–organic framework biosensing platform for detection of COVID-19 RNA. Sci Rep 14:25437. https://doi.org/10.1038/s41598-024-75668-8
16. Lee S, Lee G, Oh M (2024) MOF-on-MOF growth: inducing naturally nonpreferred MOFs and atypical MOF growth. Acc Chem Res. https://doi.org/10.1021/acs.accounts.4c00469
17. Jiang Y, Chen T-Y, Chen J-L et al (2024) Heterostructured bimetallic MOF-on-MOF architectures for efficient oxygen evolution reaction. Adv Mater 36:2306910. https://doi.org/10.1002/adma.202306910
18. Liu C, Wang J, Wan J, Yu C (2021) MOF-on-MOF hybrids: synthesis and applications. Coord Chem Rev 432:213743. https://doi.org/10.1016/j.ccr.2020.213743
19. Zhang Y, Wu J, Zhang S et al (2022) MOF-on-MOF nanoarchitectures for selectively functionalized nitrogen-doped carbon-graphitic carbon/carbon nanotubes heterostructure with high capacitive deionization performance. Nano Energy 97:107146. https://doi.org/10.1016/j.nanoen.2022.107146
20. Chai L, Pan J, Hu Y et al (2021) Rational design and growth of MOF-on-MOF Heterostructures. Small 17:2100607. https://doi.org/10.1002/smll.202100607
21. Hang X, Xue Y, Cheng Y et al (2021) From Co-MOF to CoNi-MOF to Ni-MOF: a facile synthesis of 1D Micro-/Nanomaterials. Inorg Chem 60:13168–13176. https://doi.org/10.1021/acs.inorgchem.1c01561
22. Gu C, Guo C, Li Z et al (2019) Bimetallic ZrHf-based metal-organic framework embedded with carbon dots: Ultra-sensitive platform for early diagnosis of HER2 and HER2-overexpressed living cancer cells. Biosens Bioelectron 134:8–15. https://doi.org/10.1016/j.bios.2019.03.043
23. Wang M, Hu M, Li Z et al (2019) Construction of Tb-MOF-on-Fe-MOF conjugate as a novel platform for ultrasensitive detection of carbohydrate antigen 125 and living cancer cells. Biosens Bioelectron 142:111536. https://doi.org/10.1016/j.bios.2019.111536
24. Liu X, Zheng J (2023) Highly sensitive dopamine electrochemical sensing method based on hollow dodecahedron zinc-cobalt bimetallic sulfide. Colloids Surf, A 656:130440. https://doi.org/10.1016/j.colsurfa.2022.130440
25. Gorgani L, Mohammadi M, Darzi GN, Raoof JB (2023) Electrochemical aptasensor based on bimetallic CuZr-MOF for ultrasensitive detection of miR-21. Sens Actuators, B Chem 378:133194. https://doi.org/10.1016/j.snb.2022.133194
26. Zhou N, Su F, Guo C et al (2019) Two-dimensional oriented growth of Zn-MOF-on-Zr-MOF architecture: a highly sensitive and selective platform for detecting cancer markers. Biosens Bioelectron 123:51–58. https://doi.org/10.1016/j.bios.2018.09.079
27. Tian J-Y, Lv W-C, Shen A-S et al (2023) Construction of the copper metal-organic framework (MOF)-on-indium MOF Z-scheme heterojunction for efficiently photocatalytic reduction of Cr(VI). Sep Purif Technol 327:124903. https://doi.org/10.1016/j.seppur.2023.124903
28. Leau SA, Lete C, Matei C, Lupu S (2023) Electrochemical sensing platform based on metal nanoparticles for epinephrine and serotonin. Biosensors 13:781. https://doi.org/10.3390/bios13080781
29. Banu R, Kumara Swamy BE, Jayaprakash GK, Sharma SC (2022) Simultaneous resolution of serotonin and epinephrine at poly (Victoria blue B) amplified carbon paste electrode: a voltammetric study with density functional theory evidences. Inorg Chem Commun 144:109627. https://doi.org/10.1016/j.inoche.2022.109627
30. Rantataro S, Parkkinen I, Airavaara M, Laurila T (2023) Real-time selective detection of dopamine and serotonin at nanomolar concentration from complex *in vitro* systems. Biosens Bioelectron 241:115579. https://doi.org/10.1016/j.bios.2023.115579
31. Cuhadar SN, Durmaz H, Yildirim-Tirgil N (2024) Multi-detection of seratonin and dopamine based on an electrochemical aptasensor. Chem Pap 78:7175–7185. https://doi.org/10.1007/s11696-024-03598-w